scientific reports

Check for updates

OPEN

Multimodal nomogram integrating deep learning radiomics and hemodynamic parameters for early prediction of post-craniotomy intracranial hypertension

Zunfeng Fu[1,7], Jing Wang[1,7], Wenyi Shen[1], Yanqing Wu[4], Jiajun Zhang[1], Yan Liu[1], Chongqiang Wang[1], Yanlin Shen[5], Ye Zhu[6], Weifu Zhang[3], Chunju Lv[1]✉ & Lin Peng[2]✉

To evaluate the effectiveness of deep learning radiomics nomogram in distinguishing early intracranial hypertension (IH) following primary decompressive craniectomy (DC) in patients with severe traumatic brain injury (TBI) and to demonstrate its potential clinical value as a noninvasive tool for guiding timely intervention and improving patient outcomes. This study included 238 patients with severe TBI (training cohort: *n* = 166; testing cohort: *n* = 72). Postoperative ultrasound images of the optic nerve sheath (ONS) and Spectral doppler imaging of middle cerebral artery (MCASDI) were obtained at 6 and 18 h after DC. Patients were grouped according to threshold values of 15 mmHg and 20 mmHg based on invasive intracranial pressure (ICPi) measurements. Clinical-semantic features were collected, and radiomics features were extracted from ONS images, and Additionally, deep transfer learning (DTL) features were generated using RseNet101. Predictive models were developed using the Light Gradient Boosting Machine (light GBM) machine learning algorithm. Clinical-ultrasound variables were incorporated into the model through univariate and multivariate logistic regression. A combined nomogram was developed by integrating DLR (deep learning radiomics) features with clinical-ultrasound variables, and its diagnostic performance over different thresholds was evaluated using Receiver Operating Characteristic (ROC) curve analysis and decision curve analysis (DCA). The nomogram model demonstrated superior performance over the clinical model at both 15 mmHg and 20 mmHg thresholds. For 15 mmHg, the AUC was 0.974 (95% confidence interval [CI]: 0.953–0.995) in the training cohort and 0.919 (95% CI: 0.845–0.993) in the testing cohort. For 20 mmHg, the AUC was 0.968 (95% CI: 0.944–0.993) in the training cohort and 0.889 (95% CI: 0.806–0.972) in the testing cohort. DCA curves showed net clinical benefit across all models. Among DLR models based on ONS, MCASDI, or their pre-fusion, the ONS-based model performed best in the testing cohorts. The nomogram model, incorporating clinical-semantic features, radiomics, and DTL features, exhibited promising performance in predicting early IH in post-DC patients. It shows promise for enhancing non-invasive ICP monitoring and supporting individualized therapeutic strategies.

Keywords Severe traumatic brain injury, Intracranial pressure, Ultrasound radiomics, Machine learning, Optic nerve sheath diameter(ONSD), Transcranial color doppler (TCCD), Deep learning.

Abbreviations

ALARA	As low as reasonably achievable

[1]Department of Ultrasound, The Second Affiliated Hospital of Shandong First Medical University, No. 366 Taishan Street, Taishan District, Tai'an 271000, Shandong Province, China. [2]Department of General Practice, The Second Affiliated Hospital of Shandong First Medical University, No. 366 Taishan Street, Taishan District, Tai'an 271000, Shandong Province, China. [3]Department of Public Health Management, The Second Affiliated Hospital of Shandong, First Medical University, Tai'an, China. [4]Department of Ultrasound, The Affiliated Hospital of Qilu Medical University, Xintai, China. [5]College of Medical Imaging and Laboratory, Jining Medical University, Jining, China. [6]College of Radiology, Shandong First Medical University, Tai'an, China. [7]Zunfeng Fu and Jing Wang have contributed equally to this work. ✉email: lvchunju123@163.com; penglin0125@163.com

BMI	Body mass index
CI	Confidence interval
CNN	Convolutional neural networks
CPP	Cerebral perfusion pressure
DC	Decompressive craniectomy
DCA	Decision curve analysis
DICOM	Digital imaging and communications in medicine
DTL	Deep transfer learning
DLR	Deep learning radiomics
EDV	End-diastolic velocity (MCA)
EF	Ejection fraction
GCS	Glasgow coma scale
GLCM	Gray-level co-occurrence matrix
GLRLM	Gray-level run-length matrix
GLSZM	Gray-level size zone matrix
GLDM	Gray-level dependence matrix
ICC	Intraclass correlation coefficient
ICP	Intracranial pressure
IH	Intracranial hypertension
KNN	KNEAREST neighbors
ICPi	Invasive ICP
LASSO	Least absolute shrinkage and selection operator
Light GBM	Light Gradient Boosting Machine
MCASDI	Spectral doppler imaging of middle cerebral artery
MAP	Mean arterial pressure
MCA	Middle cerebral artery
MCA_mean	Mean velocity (MCA)
MCAED	End-dystolic velocity of MCA MCA: middle cerebral artery
MCAPS	Peak systolic velocity of MCA
MCAPI	Pulse index (middle cerebral artery)
NPV	Negative predictive value
ONS	Optic nerve sheath
ONSD	Optic nerve sheath diameter
ORs	Odds ratios
PaO_2	Oxygen partial pressure (Artery)
$PaCO_2$	Carbon dioxide partial pressure (Artery)
PACS	Picture archiving and communication systems
PI	Pulse index
PPV	Positive predictive value
RF	Random forest
ROC	Receiver operating characteristic
ROI	Region of interest
TBI	Traumatic brain injury
TCD	Transcranial Doppler
TCCD	Transcranial color doppler
SNR	Signal-to-noise ratio
CNR	Contrast-to-noise ratio
PRF	Pulse repetition frequency
FPS	Frames per second

Accurate early prediction of intracranial hypertension (IH) is critical in the management of brain injury patients, as it can lead to brain herniation and pose a significant risk of irreversible brain damage and death[1,2]. Currently, a variety of invasive and non-invasive methods and devices are used for intracranial pressure (ICP) measurement[3]. Invasive monitoring is achieved by placing devices into the ventricles, brain parenchyma, epidural, subdural, and subarachnoid spaces[1,2]. Although invasive ICP monitoring (ICPi) has several disadvantages, such as the risk of infections, bleeding, catheter blockage, and brain parenchymal damage[3,4], it remains the gold standard for ICP detection due to its high accuracy. However, its high cost and technical demands mean that not all medical institutions can perform such monitoring routinely. Non-invasive techniques, such as optic nerve sheath diameter (ONSD) assessment, pupil measurement, transcranial Doppler (TCD), HeadSense technology, and flash visual evoked potential (FVEP), are also used to assess ICP. While ONSD and TCD have demonstrated moderate to good accuracy in related studies[5–7], they are not yet able to completely replace invasive ICP monitoring in the short term.

The American Brain Injury Foundation recommends ICP monitoring for all traumatic brain injury (TBI) cases with a Glasgow Coma Scale (GCS) score between 3 and 8, and abnormal CT findings (such as hematoma, contusion, severe swelling, brain herniation, or basal cistern collapse)[8]. However, for patients after initial craniotomy, there is controversy regarding whether to implement invasive ICP monitoring, even if they meet the criteria for ICP monitoring. Proponents argue that invasive monitoring is necessary for maintaining adequate cerebral perfusion pressure (CPP). Without ICP monitoring, it would be difficult to develop and implement CPP-guided treatment protocols. Studies have shown that a significant proportion of TBI patients still have

elevated ICP after undergoing decompressive craniectomy (DC), potentially causing CPP to drop to dangerously low levels (< 60 mmHg). Therefore, ICP monitoring is considered essential for these patients, as it provides crucial data for CPP-based therapeutic decisions[9,10]. Conversely, opponents argue that routine ICP monitoring is unnecessary. They believe that experienced clinicians can use pressure measurements from the decompression window, combined with CT or MRI scans, to identify recurrent hematomas, fluid accumulation, and changes in the size and shape of the ventricles, thereby estimating ICP levels and conducting a comprehensive ICP assessment. Furthermore, they point out that there is no consensus on the threshold for ICP after DC. Additionally, for severely injured TBI patients, maintaining ICP below 20 mmHg does not offer a significant advantage over treatment protocols based on imaging and clinical examination alone[11,12]. Despite the differences in opinion, the importance of maintaining normal ICP in post-DC patients is undeniable, and mature, reliable non-invasive monitoring techniques may hold the key to resolving this debate in the future. In our previous research[13], our team demonstrated that the combined use of ONSD by ultrasound and transcranial color doppler (TCCD) has good clinical application value, outperforming single indicators in discriminating early IH. However, for patients with mild IH (ICP ≥ 15 mmHg), the predictive sensitivity was only 0.484, (95% confidence interval [CI]:0.358–0.613) through this combined clinical method [Area Under the Curve (AUC):0.732, 95% CI: (0.651–0.822)], which warrants further investigation into optimizing predictive models to improve the monitoring of early mild IH.

Radiomics is a quantitative analytical approach that allows for the extraction and evaluation of radiological features from the entire lesion, enhancing the accuracy and objectivity of disease diagnosis and treatment outcome prediction[14]. Deep learning can quantify high-dimensional radiological phenotypes beyond human perception and develop specialized predictive models for diverse clinical applications, making it a valuable non-invasive tool for prognostic assessment[15], disease diagnosis[16], and treatment decision-making[17]. Nevertheless, research evidence remains insufficient to establish the feasibility of using deep learning techniques to predict early IH in post-DC patients with TBI. This study aims to develop a deep learning model based on ultrasound images to enhance the accuracy of IH prediction in these patients. Additionally, the study evaluates the predictive value of individual ONS images, individual middle cerebral artery spectral Doppler imaging (MCASDI) images, and their pre-fused images within the comprehensive model.

Materials and methods

Patient population

This retrospective observational study was conducted at the Neuro-Intensive Care Unit (NICU) of the Second Affiliated Hospital of Shandong First Medical University (SFMU) between May 2018 and December 2024 and at the NICU of the Affiliated Hospital of Qilu Medical University between August 2019 and December 2024. Due to the retrospective nature of the study, the Ethics Committee of the Second affiliated Hospital of SFMU waived the need of obtaining informed consent.

A total of 238 patients with TBI who underwent primary DC were included based on predefined inclusion and exclusion criteria (Fig. 1: Flowchart for Selecting the Study Population). The study enrolled adult patients (≥ 18 years old) with TBI who had undergone primary DC and required ICP monitoring within 24 h postoperatively.

Exclusion criteria included patients with poor TCCD window quality that impaired 2D imaging—specifically, cases where the temporal bone window could not be penetrated by ultrasound to detect the MCA, or where vascular boundaries appeared blurred and the signal-to-noise ratio (SNR) and contrast-to-noise ratio (CNR) were reduced, compromising diagnostic reliability. Patients with significant cardiovascular or cerebrovascular conditions, such as severe arrhythmias, critical valvular stenosis, moderate to severe cerebral vasospasm, or ICPi fluctuations exceeding 10 mmHg within 24 h, were also excluded. Eligible patients—176 from the Second Affiliated Hospital of SFMU and 62 from the Affiliated Hospital of Qilu Medical University—were randomly allocated to the training and testing cohorts at a 7:3 ratio.

Treatment methods

In patients with TBI, the decision to perform primary DC is influenced by factors such as the injury mechanism, clinical symptoms, GCS score, and findings on CT imaging. Unilateral DC is typically performed when hematomas are limited to a single hemisphere, whereas bilateral or frontotemporal decompression is preferred in cases involving bilateral hematomas or frontal lobe damage. Surgically, a bone flap approximately 9 × 9 cm is created and extended in an arc to adequately expose the dura mater. Hemostasis is achieved by evacuating hematomas, necrotic brain tissue, and clots. The dura is then either loosely sutured or covered with a synthetic substitute. ICP is continuously monitored via an intraparenchymal sensor or a ventricular catheter linked to an external transducer. The probe placement depends on the lesion location—on the same side for unilateral lesions, or on the right hemisphere in cases of diffuse injury.

ICP management in this study followed the Chinese Expert Consensus on the Monitoring and Management of Elevated ICP. Sedation was maintained using agents such as propofol, titrated based on electroencephalography to achieve burst suppression. When partial neurological evaluation was required, midazolam or dexmedetomidine were administered with individualized dosing. Sedation depth and ICP were continuously monitored, with sedation typically maintained for 24–72 h postoperatively. CPP was kept between 60 and 70 mmHg, adjusted based on optimal CPP, and supported by vasopressors like norepinephrine to maintain MAP. For hyperosmolar therapy, 3% hypertonic saline (2–5 mL/kg over 15–30 min) and mannitol (0.25–1 g/kg over 20–30 min) were used, with serum osmolality (< 320 mOsm/L) and renal function continuously monitored. Hypertonic Saline was preferred during acute ICP elevation (ICP > 20 mmHg), with repeat doses at 4–6 h intervals if necessary. Therapeutic hypothermia (33–35 °C for 24–72 h) was induced gradually (0.25–0.5 °C/h), with rewarming performed slowly (0.1–0.25 °C/h) to avoid rebound ICP elevation. Core temperature, ICP, CPP, and electrolytes

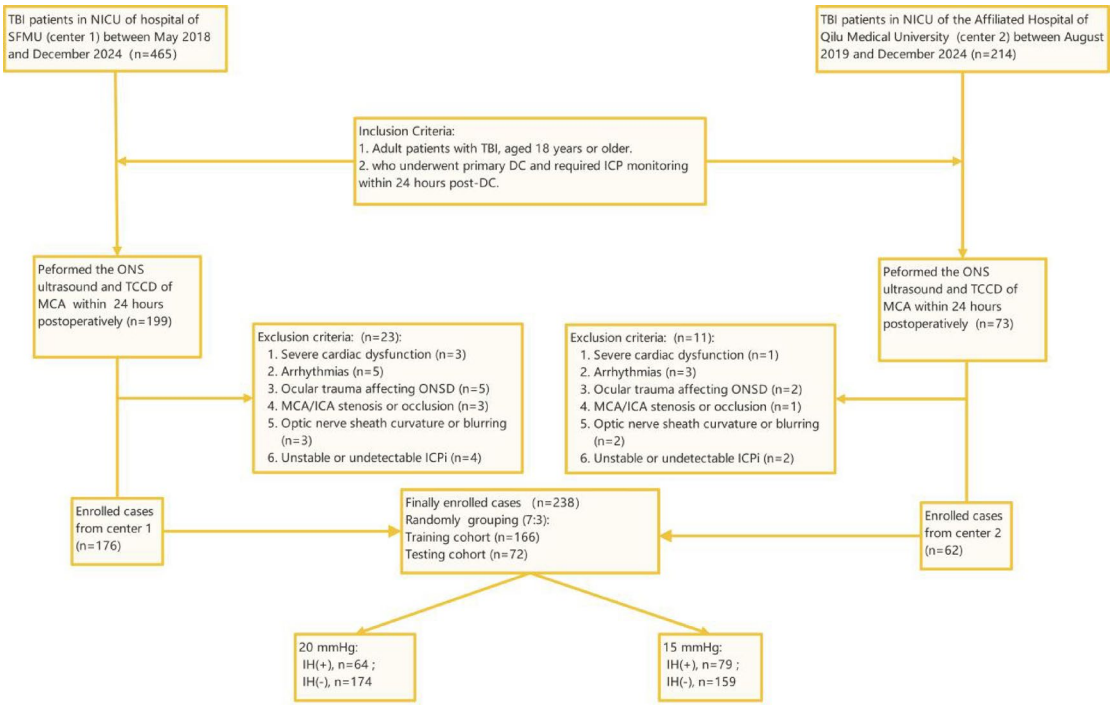

Fig. 1. Flowchart of study population selection. SFMU, Shandong First Medical University; MCA, middle cerebral artery; ONS, optic nerve sheath; TCCD, transcranial color Doppler; IH, intracranial hypertension; TBI, traumatic brain injury; ICA, internal carotid artery; post-DC, postoperative decompressive craniectomy; ICP, intracranial pressure.

were continuously monitored. All interventions were adjusted dynamically based on multimodal monitoring, balancing clinical benefit with risks such as infection or coagulopathy.

In the absence of universally accepted guidelines for IH post-DC, thresholds of 15 mmHg (indicating mild elevation) and 20 mmHg (indicating moderate to severe elevation) were adopted to assess the model's predictive capability at these levels.

US acquisition, semantic features, and segmentation

ONS imaging was performed twice within 24 h in post-DC patients using the Mindray M9 ultrasound system equipped with an L12-4s linear probe (5–10 MHz; Shenzhen, Guangzhou, China). Patients were positioned in a supine posture, and the probe was gently placed on the closed upper eyelid with standard coupling gel, angled to visualize the ONS in the transverse plane. ONSD measurements were obtained 3 mm posterior to the optic disc, with three measurements taken in the transverse plane for each eye to reduce variability.

To ensure both image quality and safety, the probe frequency was set to 10 MHz, providing an optimal balance between resolution and tissue penetration. The power output was maintained at 20–25%, in accordance with the "As Low As Reasonably Achievable" (ALARA) principle and within recommended safety limits (MI ≤ 0.23, TI ≤ 1 °C, and ISPTA.3 ≤ 50 mW/cm^2). The depth was adjusted to 40–45 mm to center the eyeball within the field of view, and the focus was set at 25–30 mm, aligning with the typical position of the optic nerve. To enhance image clarity, the gain was set to 55–60%, ensuring adequate brightness without introducing excessive contrast. For Doppler imaging, a pulse repetition frequency (PRF) of 1.0 kHz was used. A frame rate of 25 frames per second (FPS) was maintained to ensure resolution. All measurements were performed using the same type of probe across patients to maintain consistency and comparability.

Additionally, MCASDI captured by bedside TCCD and assessments were conducted using the same Mindary M9 ultrasound system, equipped with an SP5-1s probe (1–5 MHz). Bilateral MCA evaluation included the measurement of pulse index (PI), peak systolic velocity (PSV), end-diastolic velocity (EDV), and mean velocity (MV). The definitive PI value was determined by averaging the measurements from both sides or selecting the higher value in cases of significant discrepancy.

For TCCD assessments, a phased-array probe with a frequency of 1.6 MHz was used to ensure adequate acoustic penetration through the temporal bone window. The imaging depth was set between 12 and 16 cm to visualize the basal cerebral arteries, and the focal zone was positioned at 5–7 cm, corresponding to the depth of the circle of Willis. The gain was adjusted to 60–70% to achieve optimal image brightness while minimizing background noise. Additionally, a frame rate of 25 FPS was maintained to ensure resolution. The PRF was set to 3 kHz to allow for accurate detection of cerebral blood flow velocities without aliasing.

Two ultrasound specialists (ZJJ and WCQ), who were blinded to the ICPi values and clinical information, independently assessed the ONS and TCCD images. One specialist had 4 years of experience, while the other had

15 years of expertise in ultrasound imaging. Both specialists underwent standardized training for measurements and reached a consensus on their evaluations of the images.

Ultrasound images were preprocessed by converting them from digital imaging and communications in medicine (DICOM) format to a compatible format, resizing them to a uniform 512 × 512 pixel resolution, and applying z-score normalization to standardize pixel intensities. These steps ensured consistent image quality and facilitated accurate feature extraction and model training.

The regions of interest (ROIs) were manually delineated by ultrasound imaging experts using ITK-SNAP (version 3.8.0, http://www.itksnap.org/). The experts were blinded to the ICPi values, and any discrepancies were resolved through consensus discussion. Intra- and inter-observer reproducibility were assessed using the intraclass correlation coefficient (ICC), with values ≥ 0.75 considered to indicate strong reliability. Figure 2 illustrates the flowchart depicting the overall research design.

Radiomics and DTL feature extraction

Radiomic features were extracted from the segmented ROIs using PyRadiomics (version 3.0.1, http://pyradiomics.readthedocs.io). The extracted features were categorized into three primary groups: (I) geometry, (II) intensity, and (III) texture. Geometric features describe the two-dimensional shape of the ONS, while intensity features reflect the statistical distribution of voxel intensities within the ONS. These intensity features capture the first-order statistical distribution of voxel intensities, providing insights into the overall brightness and contrast of the ONS. Texture features, on the other hand, characterize the patterns and spatial distribution of intensities at higher orders, offering further details on the internal structure of the ONS. A comprehensive list and detailed explanation of the extracted radiomic features can be found in Supplementary S1.

The ResNet101 architecture was adapted to develop a convolutional neural network (CNN) for extracting deep transfer learning (DTL) features. To achieve this, separate CNN models were pretrained using ONS images, MCASDI images, and a combined dataset containing both ONS and MCASDI images. After feature extraction, the DTL features from ONS and MCASDI images were fused using feature concatenation, where the extracted feature vectors from each modality were directly combined to form a comprehensive representation. Specifically, the output from the penultimate layer of each pretrained CNN model was concatenated to generate the final DTL feature set, ensuring an integrated representation of both imaging modalities.

To fine-tune ResNet101 and reduce overfitting, we applied a dropout rate of 0.5 and L2 regularization with a coefficient of 0.001. The initial learning rate was set to 0.0001 and adjusted using a cosine annealing strategy. Additionally, we used data augmentation techniques during training, including random horizontal and vertical flipping, slight rotations (± 5°), and brightness adjustments (± 10%), to improve model robustness and generalizability.

Radiomics and DTL feature selection

The z-score normalization technique was applied to standardize all features. A statistical analysis was then performed using the Mann–Whitney U test, with features selected based on their p-values. Only features with a p-value < 0.05 were retained. Spearman's rank correlation coefficient was calculated to assess the correlation of features with high repeatability. If two features had a correlation coefficient greater than 0.9, one was excluded. The signature construction from the discovery dataset employed Least Absolute Shrinkage and Selection Operator (LASSO) regression. LASSO regression uses a regularization weight, λ, to shrink regression coefficients towards zero, assigning zero to irrelevant features. The optimal value of λ was determined via 5-fold cross-validation, selecting the value that minimized the cross-validation error. The scikit-learn package (version 1.0.2) in Python was utilized for LASSO regression modeling. Subsequently, all selected features were used to train a Light Gradient Boosting Machine (LightGBM), with hyperparameters set as follows: learning rate = 0.1, maximum

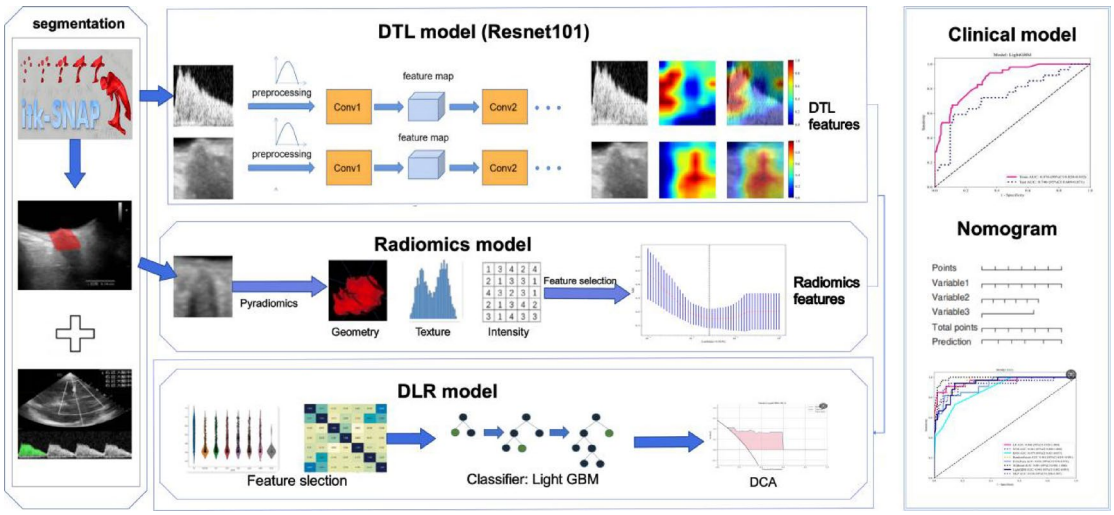

Fig. 2. Workflow of radiomic analysis in this study.

depth = 6, and number of leaves = 31. To avoid data leakage and ensure the integrity of model evaluation, all feature selection procedures were performed exclusively on the training dataset. The independent testing cohort was strictly reserved for external validation and was not involved in any stage of feature selection or model training.

Statistical analyses

Statistical analyses were performed using MedCalc (version 20.015.0), Python (version 3.7.11; http://www.python.org). Student's t-test and ANOVA were applied to compare continuous variables, expressed as mean ± standard deviation (χ ± s). The chi-square test or Fisher's exact test was used to analyze categorical variables, presented as ratios. A p-value of less than 0.05 was considered statistically significant.

Results

Patients' population and clinical-ultrasonic characteristics

A total of 238 patients, including 159 males and 79 females, participated in the study. At an ICP threshold of 15 mmHg, the incidence of intracranial hypertension (IH) was 33.19%, while at 20 mmHg, it was 26.89%. Among these patients, 166 were randomly assigned to the training set, and 72 to the test set.

No significant differences were observed between the cohorts in terms of age, weight, height, BMI, gender, ejection fraction (EF), MAP, partial pressure of oxygen (PaO_2), partial pressure of carbon dioxide ($PaCO_2$), heart rate, or respiratory rate, as outlined in Table 1 (ICP threshold of 15 mmHg) and Supplementary Table 1S (ICP threshold of 20 mmHg). Significant differences were observed in PI and ONSD between the normal and elevated ICP groups in both the training and validation sets. Univariate and multivariable logistic regression analyses further identified MCAPI and ONSD as significant predictors (see Table 2 and Supplementary Table 2S). These variables were subsequently incorporated into the clinical predictive model.

Patients with elevated ICP (≥ 15 mmHg) exhibited a higher likelihood of increased PI (odds ratio [OR]: 4.911; 95% CI: 1.777–13.578) and elevated ONSD (OR: 7.320; 95% CI: 3.386–15.841). A similar trend was observed at the 20 mmHg ICP threshold, with increased PI (OR: 4.976; 95% CI: 1.840–13.454) and elevated ONSD (OR: 4.302; 95% CI: 2.204–8.410).

Feature selection and deep learning radiomics model construction

Radiomic features were extracted from the segmented ROIs using the PyRadiomics software (version 3.0.1), yielding a total of 1,561 commonly used features. To ensure reliability, a reproducibility assessment was conducted using intraclass correlation coefficients (ICCs), which confirmed 1,291 and 1,059 features as reliable at thresholds of 15 mmHg and 20 mmHg, respectively. Subsequently, the Mann–Whitney U test identified

Variables	Training cohort (*n* = 166)			*P* value	Testing cohort (*n* = 72)			*P* value
	All	Normal (*n* = 116)	Elevated ICPi (≥ 15mmHg) (*n* = 50)		All	Normal (*n* = 43)	Elevated ICPi (≥ 15mmHg) (*n* = 29)	
Age (years)	61.24 ± 10.66	60.91 ± 10.68	62.02 ± 10.68	0.66	61.79 ± 10.04	61.91 ± 9.89	61.62 ± 10.43	0.90
Weight (kg)	75.09 ± 10.68	74.57 ± 11.32	76.30 ± 9.03	0.59	75.60 ± 12.23	76.30 ± 12.49	74.55 ± 11.99	0.47
Height(cm)	168.46 ± 7.02	168.09 ± 6.86	169.32 ± 7.39	0.30	170.00 ± 8.49	170.95 ± 8.70	168.59 ± 8.10	0.24
BMI (kg/m^2)	26.43 ± 2.86	26.35 ± 3.11	26.61 ± 2.19	0.79	26.05 ± 3.07	26.00 ± 3.13	26.13 ± 3.04	0.86
EF (%)	0.63 ± 0.05	0.63 ± 0.06	0.64 ± 0.05	0.39	0.62 ± 0.05	0.63 ± 0.05	0.61 ± 0.06	0.37
MCAPI	1.16 ± 0.55	1.04 ± 0.33	1.45 ± 0.81	< 0.001	1.20 ± 0.46	1.09 ± 0.41	1.35 ± 0.49	0.0029
MAP (mm Hg)	87.17 ± 7.80	87.35 ± 7.68	86.74 ± 8.15	0.59	86.85 ± 8.11	85.47 ± 6.57	88.90 ± 9.73	0.300
ONSD (mm)	4.76 ± 0.52	4.62 ± 0.39	5.09 ± 0.64	< 0.001	4.76 ± 0.44	4.59 ± 0.30	5.03 ± 0.49	< 0.001
PaO_2 (mm Hg)	119.44 ± 24.72	121.81 ± 25.90	113.94 ± 20.95	0.059	121.74 ± 24.40	124.00 ± 24.10	118.38 ± 24.88	0.34
$PaCO_2$ (mm Hg)	35.06 ± 2.75	34.97 ± 2.70	35.26 ± 2.87	0.78	35.06 ± 2.23	34.98 ± 2.21	35.17 ± 2.28	0.64
Breath (bpm)	20.36 ± 2.87	20.29 ± 2.83	20.50 ± 3.00	0.62	20.43 ± 3.14	19.74 ± 2.78	21.45 ± 3.42	0.06
Beats (bpm)	84.37 ± 8.19	84.40 ± 7.64	84.30 ± 9.42	0.94	83.75 ± 8.67	82.72 ± 7.81	85.28 ± 9.74	0.22
MCA_mean (cm/s)	62.53 ± 22.64	64.88 ± 21.30	57.09 ± 24.84	0.043	61.41 ± 20.30	62.64 ± 19.66	59.59 ± 21.42	0.44
MCAPS (cm/s)	105.16 ± 28.59	104.89 ± 25.70	105.78 ± 34.66	0.88	108.00 ± 27.68	105.79 ± 26.73	111.28 ± 29.20	0.41
MCAED (cm/s)	38.20 ± 14.66	40.80 ± 13.54	32.16 ± 15.49	< 0.001	38.80 ± 13.64	40.78 ± 14.16	35.86 ± 12.48	0.134
Sex				0.19				0.73
Male	109(65.66)	72(62.07)	37(74.00)		50(69.44)	31(72.09)	19(65.52)	
Female	57(34.34)	44(37.93)	13(26.00)		22(30.56)	12(27.91)	10(34.48)	

Table 1. Baseline characteristics of patients in cohorts. *Indicates $p < 0.05$. Numerical data are presented as mean ± standard deviation; categorical data are shown as number (percentage). bpm, breaths per minute or beats per minute; MCAED, end-diastolic velocity of the middle cerebral artery; EF, ejection fraction; MAP, mean arterial pressure; MCA, middle cerebral artery; MCA_mean, mean velocity of the MCA; $PaCO_2$, arterial partial pressure of carbon dioxide; PI, pulsatility index of the MCA; PaO_2, arterial partial pressure of oxygen; MCAPS, peak systolic velocity of the MCA; ONSD, optic nerve sheath diameter.

Variable	Univariate analysis OR (95% CI)	*P* value	Multivariate analysis OR((95% CI)	*P* value
Beats (bpm)	0.985 (0.978–1.044)	0.532		
BMI (kg/m^2)	0.977 (0.931–1.121)	0.650		
Breath (bpm)	1.017 (0.989–1.186)	0.084		
EF (%)	0.224 (0.001–33.850)	0.558		
Height (cm)	0.988 (0.968 to 1.040)	0.854		
Weight (kg)	0.991 (0.981–1.029)	0.685		
MAP (mm Hg)	0.993 (0.977–1.045)	0.525		
MCA_mean (cm/s)	0.983 (0.973–0.999)	0.039*	1.011 (0.991–1.032)	0.2832
MCAED(cm/s)	0.966 (0.941–0.982)	0.000*	0.975 (0.942–1.009)	0.156
MCAPI	8.296(3.008–14.980)	< 0.0001*	4.911 (1.777–13.578)	0.000*
MCAPS (cm/s)	1.001 (0.993–1.013)	0.493		
ONSD(mm)	7.856 (4.294–19.876)	0.000*	7.320 (3.386–15.841)	0.000*
$PaCO_2$ (mmHg)	0.979 (0.935–1.152)	0.478		
PaO_2 (mmHg)	0.984 (0.977–0.999)	0.045*	0.993 (0.980–1.006)	0.2946
Sex	0.855 (0.421–1.355)	0.347		
Age	0.999 (0.980–1.033)	0.628		

Table 2. Univariate and multivariable logistic regression analyses for selecting clinical features of model development (15 mmHg). *Indicates $p < 0.05$. bpm, breaths per minute or beats per minute; MCAED, end-diastolic velocity of the middle cerebral artery; EF, ejection fraction; MAP, mean arterial pressure; MCA, middle cerebral artery; MCA_mean, mean velocity of the MCA; $PaCO_2$, arterial partial pressure of carbon dioxide; MCAPI, pulsatility index of the MCA; PaO_2, arterial partial pressure of oxygen; MCAPS, peak systolic velocity of the MCA; ONSD, optic nerve sheath diameter.

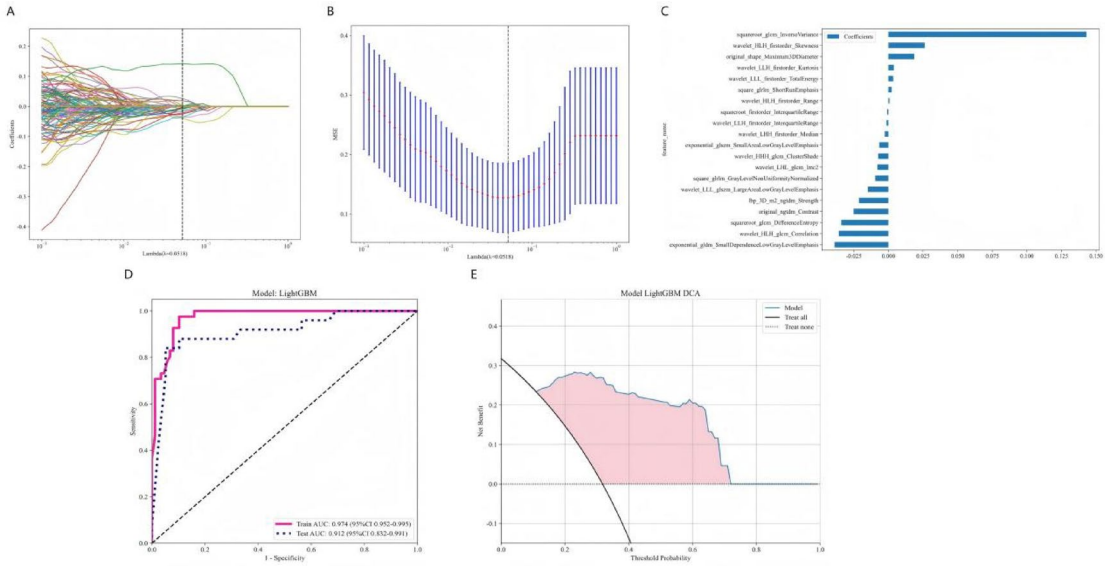

Fig. 3. Radiomics feature selection and model performance evaluation using the LASSO algorithm (15mmHg). (A) Coefficient profiles of radiomics features generated by the LASSO algorithm, with each colored line representing an individual feature. (B) Selection of the optimal regularization parameter (λ) via cross-validation in the LASSO model. (C) Weight coefficients of the features retained after LASSO selection. (D) Receiver operating characteristic (ROC) curves illustrating the predictive performance of the radiomics signature in both training and testing sets. (E) DCA assessing the clinical utility of the radiomics signature model. Abbreviations: LASSO, least absolute shrinkage and selection operator; ROC, receiver operating characteristic; DCA, decision curve analysis.

1,023 and 906 statistically significant features. Further refinement was performed using the Spearman rank correlation test, narrowing the selection to 280 and 237 features. The Rad score was then computed using a LASSO regression model, which identified 20 and 26 features with nonzero coefficients. The coefficients and mean standard errors (MSE) from 5-fold cross-validation are shown in Figs. 3A and B. Figure 3C presents the

coefficient values of the selected nonzero features at the 15 mmHg threshold, while Supplementary Fig. 3S(A–C) displays the corresponding results for 20 mmHg. The radiomics signature model demonstrated robust predictive performance, achieving AUC values of 0.974 (95% CI: 0.952–0.995) and 0.912 (95% CI: 0.832–0.991) in the training and testing cohorts at 15 mmHg, and 0.943 (95% CI: 0.902–0.983) and 0.887 (95% CI: 0.801–0.973) at 20 mmHg, as shown in Figs. 3D and Supplementary 3SD.

To enhance predictive accuracy for early IH in post-DC patients, radiomic features were combined with DTL features. This fusion strategy incorporated DLR features for further analysis. Using the LASSO regression model, 14 and 26 features with nonzero coefficients were selected at thresholds of 15 mmHg and 20 mmHg, respectively. The coefficients and mean standard errors from 5-fold cross-validation are presented in Figs. 4A and B for 15 mmHg and Supplementary Figs. 4SA and SB for 20 mmHg. Figures 4C and Supplementary 4 SC illustrate the coefficient values of the final selected features for 15 mmHg and 20 mmHg, respectively. The DLR-radiomics signature model achieved AUC values of 0.927 (95% CI: 0.896–0.958) and 0.885 (95% CI: 0.779–0.992) in the training and testing cohorts at 15 mmHg, and 0.949 (95% CI: 0.915–0.983) and 0.893 (95% CI: 0.801–0.985) at 20 mmHg, as demonstrated in Fig. 4D and Supplementary 4SD. Decision curve analysis (DCA) for the radiomics and DLR-radiomics signature models is presented in Figs. 3E and 4E for 15 mmHg and Supplementary Figs. 3SE and 4 SE for 20 mmHg.

Clinical model and nomogram model construction

The clinical model demonstrated strong predictive performance, achieving AUC values of 0.868 (95% CI: 0.812–0.923) and 0.807 (95% CI: 0.705–0.909) in the training and testing cohorts at 15 mmHg, and 0.891 (95% CI: 0.842–0.940) and 0.814 (95% CI: 0.691–0.937) at 20 mmHg, respectively, as shown in Fig. 5A and Supplementary Fig. 5SA. DCA confirmed the model's net benefit in predicting IH, as depicted in Figs. 5B and Supplementary 5SB for 15 and 20 mmHg. Additionally, Fig. 6 and Supplementary 6S present nomograms designed for clinical application, where the total score corresponds to the probability of IH in post-DC patients within 24 h at different thresholds.

Comparison of the clinical model, DTL-radiomics model, and nomogram model

The performance of the clinical, radiomics, DTL, DLR-radiomics, and nomogram models is summarized in Table 3 (15 mmHg) and Supplementary Table 3S (20 mmHg). At the 15 mmHg threshold, AUC values in the training cohort (Fig. 7A) were as follows: 0.860 (95% CI:0.796–0.925) for the clinical model, 0.974 (95% CI:0.952–0.995) for the radiomics model, 0.946 (95% CI:0.908–0.984) for the DTL model, 0.973 (95% CI:0.951–0.994) for the DLR model, and 0.974 (95% CI:0.953–0.995) for the nomogram model. In the testing cohort (Fig. 7D), the AUC values were 0.801 (95% CI:0.689–0.913) for the clinical model, 0.912 (95% CI: 0.832–0.991) for the radiomics model, 0.850 (95% CI:0.747–0.956) for the DTL model, 0.914 (95% CI:0.835–0.994) for the

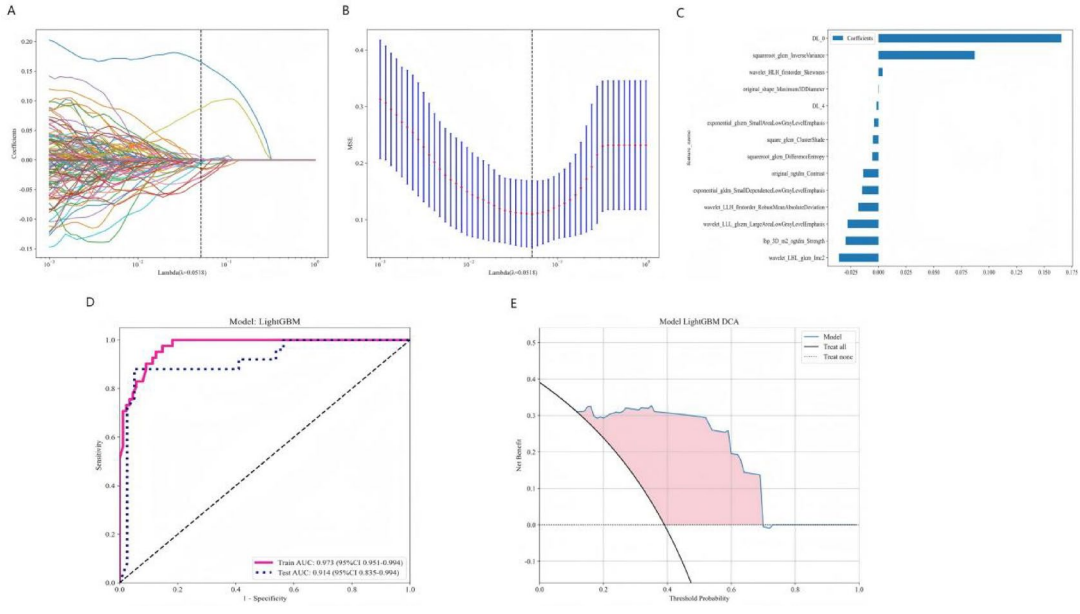

Fig. 4. DLR features selection using the LASSO algorithm and performance assessment of the DLR signature model (15mmHg). (A) LASSO-derived coefficient profiles for radiomics features, with each colored line representing an individual feature. (B) Optimal value of the regularization parameter (λ) determined via cross-validation. (C) Weight coefficients of features selected by the LASSO algorithm. (D) ROC curves demonstrating the classification performance of the DTL-radiomics signature in both training and testing datasets. (E) Decision curve analysis (DCA) evaluating the clinical benefit of the DTL-radiomics model. LASSO, least absolute shrinkage and selection operator; ROC, receiver operating characteristic; DCA, decision curve analysis.

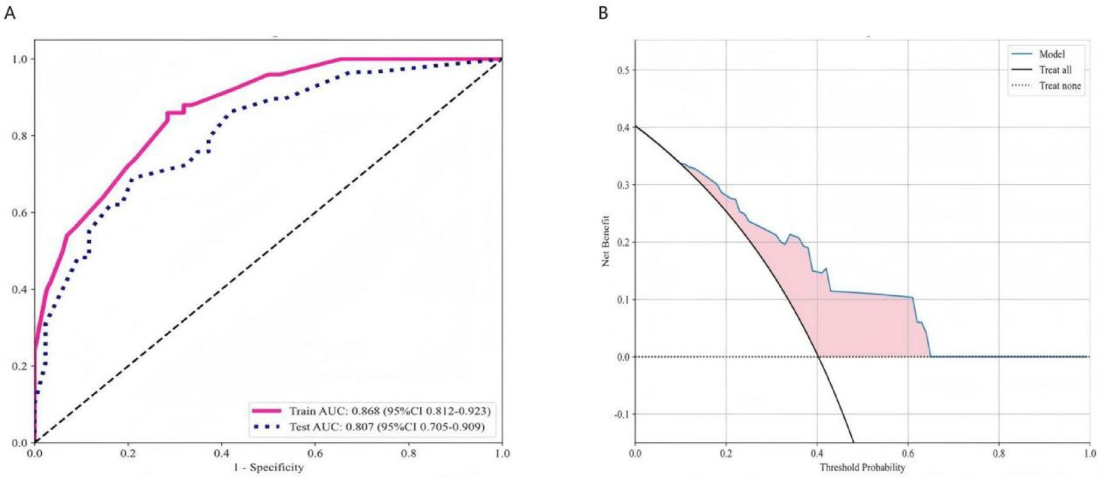

Fig. 5. The establishment and performance of the clinical model (15mmHg). (A) Displays the ROC curves of the clinical model within both the training and testing cohorts. (B) Presents the DCA results for the clinical model. ROC, receiver operating characteristic; DCA, decision curve analysis.

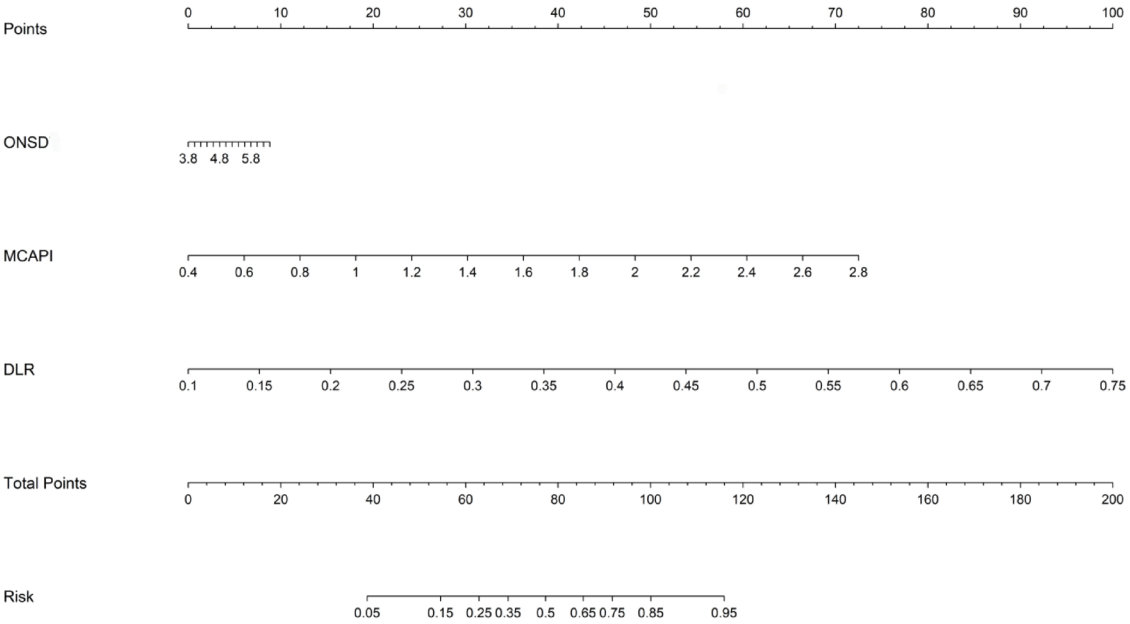

Fig. 6. Clinical application of the nomogram for predicting early intracranial hypertension (IH) in post-decompressive craniectomy (post-DC) patients (15 mmHg threshold). (1) Variable names on the left ('*ONSD*, *MCAPI*, and *DLR*') correspond to scales on horizontal lines, indicating the range of values each variable can take. The length of each line reflects its relative contribution to the risk of IH (defined as ICP ≥ 15 mmHg). (2) '*Points*' refers to the score assigned to each variable based on its value; '*Total Points*' is the sum of all individual scores. (3) Predicted Probability (labeled as *'Risk'*) shows the estimated probability of IH based on the total score. ONSD, optic nerve sheath diameter; MCAPI, pulsatility index of the middle cerebral artery; DLR, deep learning radiomics; IH, intracranial hypertension; DC, decompressive craniectomy.

DLR model, and 0.919 (95% CI:0.846–0.993) for the nomogram model. Decision curve analysis (DCA) results for these models are presented in Figs. 7B and E, with similar patterns observed at the 20 mmHg threshold in Supplementary Fig. 7S (A, B, D, E).

The results indicate that, in the training cohort, the nomogram, DLR, and radiomics models provided greater net clinical benefit in predicting IH compared to the clinical model. The calibration curves (Fig. 7C and F; Supplementary Fig. 7SC and SF) demonstrate good concordance between predicted and observed IH in both the training and testing cohorts. The Hosmer–Lemeshow test results were not statistically significant in either cohort (training: $p = 0.386$; testing: $p = 0.131$), supporting the models' calibration accuracy. Furthermore, the DeLong test showed that the nomogram significantly outperformed the clinical model at the 15 mmHg

Signature	Accuracy	AUC	95% CI	Sensitivity	Specificity	PPV	NPV	Cohort
Clinic								
	0.775	0.868	0.796–0.925	0.756	0.784	0.62	0.873	Train
	0.750	0.801	0.689–0.913	0.640	0.821	0.696	0.780	Test
Rad								
	0.915	0.974	0.952–0.995	0.951	0.898	0.812	0.975	Train
	0.891	0.912	0.832–0.991	0.800	0.949	0.909	0.881	Test
DTL								
	0.881	0.946	0.908–0.984	0.878	0.841	0.719	0.936	Train
	0.783	0.850	0.747–0.956	0.759	0.897	0.826	0.854	Test
DLR								
	0.884	0.973	0.951–0.994	0.951	0.852	0.75	0.974	Train
	0.906	0.914	0.835–0.994	0.840	0.949	0.913	0.902	Test
Nomogram								
	0.907	0.974	0.953–0.995	0.951	0.886	0.796	0.975	Train
	0.891	0.919	0.846–0.993	0.84	0.923	0.875	0.9	Test

Table 3. The performance of five models in the training and testing cohort (15 mmHg). DTL, deep transfer learning; AUC, area under curve; CI, confidence interval. DLR, Deep Learning Radiomics.

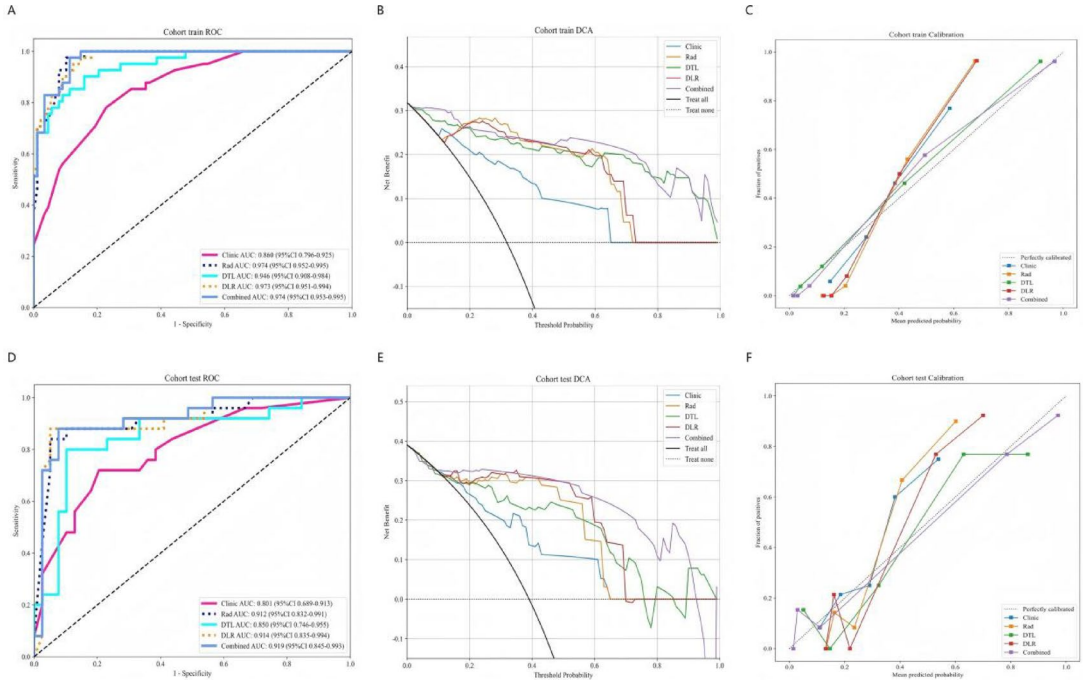

Fig. 7. AUC, DCA and Calibration curves of clinical, DTL, DLR and nomogram models at the 15 mmHg threshold in the training cohort (A, B, C) and the testing cohort (D, E, F).

threshold in both the training ($p = 0.000$) and testing ($p = 0.004$) cohorts. At the 20 mmHg threshold, however, the nomogram demonstrated superior performance only in the training cohort ($p = 0.003$), with no significant improvement observed in the testing cohort ($p = 0.525$). This difference may be due to the limited additional information contributed by the DLR model when combined with clinical features for predicting moderate to severe IH in the testing cohort.

This study also assessed the performance of DLR models constructed using ONS images, MCASDI images, and their concatenation-based feature fusion. At the 15 mmHg threshold, the DLR(ONS) model [AUC: 0.914 (95% CI:0.835–0.994)] exhibited comparable predictive performance to the DLR (feature-fused) model (0.913, 95% CI:0.832–0.994) and the DLR (MCASDI) model (0.873, 95% CI:0.757–0.989) in the testing cohort. Similarly, at the 20 mmHg threshold, the AUC values in the testing cohort were 0.893 (95% CI:0.801–0.985), 0.889 (95% CI:0.810–0.965) and 0.870 (95% CI:0.751–0.988), respectively. These findings indicate that concatenation-based feature pre-fusion of ONS and MCASDI images did not provide a substantial improvement in predictive

performance over the DLR(ONS) model alone. Therefore, all images and tables presented in this study are based on features extracted from ONS images.

Discussion

This study utilized deep learning-based radiomic features to develop a nomogram model for accurately predicting the risk of early IH in post-DC patients. By integrating radiomic and DTL features with clinical parameters, the nomogram model demonstrated stronger performance compared to the clinical model at both 15 mmHg and 20 mmHg thresholds. For 15 mmHg, the AUC was 0.974 (95% CI: 0.953–0.995) in the training cohort and 0.919 (95% CI: 0.845–0.993) in the testing cohort. For 20 mmHg, the AUC was 0.968 (95% CI: 0.944–0.993) in the training cohort and 0.889 (95% CI: 0.806–0.972) in the testing cohort. Furthermore, its capability to assess IH using postoperative ultrasound scans provides valuable support for early intervention and treatment planning.

Previous studies[18] have shown that ultrasound measurement of ONSD is a highly effective method for detecting IH following TBI or other causes. The AUC for this technique is 0.940 (95% CI: 0.91–0.96), whereas TCD demonstrates relatively poor performance in detecting IH, with AUC values ranging from 0.55 to 0.72 across different studies. Notably, both ONSD and TCD-derived parameters hold promise due to their ease of use, bedside feasibility, and cost-effectiveness[6]. However, most prior researches have focused on patients who did not undergo DC after TBI, with limited studies examining post-DC patients. This gap is partly due to the altered intracranial physiology in post-DC patients, which deviates from the classical Monroe–Kellie doctrine and complicates the application of conventional ICP assessment methods. Following DC, intracranial contents protrude through the decompressed bone window, disrupting the original ICP equilibrium and impairing the autoregulatory function of cerebral blood vessels. Consequently, conventional ICP thresholds, such as 20, 22 or 25 mmHg, are no longer applicable to these patients. Furthermore, the clinical utility of TCD-derived parameters, including the PI, EDV of MCA, and non-invasive ICP estimation formulas, has been questioned.

Several studies[19,20] have attempted to correlate post-DC ONSD changes with ICP through observational methods. However, this approach is highly operator-dependent, as ONSD measurements are influenced by factors such as ultrasound probe selection, measurement plane, and patient positioning. These methodological inconsistencies limit the scalability of this technique in clinical practice. Our previous research found that the AUC for predicting IH (≥ 20 mmHg) using ONSD alone was 0.74, and for an ICP threshold of 15 mmHg, it was 0.73[13]. These findings highlight the limitations of relying on a single clinical parameter for non-invasive ICP monitoring in post-DC patients. In the current study, we developed a clinical model that integrates ONSD and TCCD-derived parameters to predict IH. The AUC for predicting IH at 20 mmHg was 0.85, while at 15 mmHg, it was 0.79. Additionally, for the first time, we applied radiomics and deep learning techniques to ultrasound images of the ONS and the MCASDI for non-invasive ICP monitoring in post-DC patients. The nomogram model achieved strong predictive ability, with consistent results across both training and testing datasets.

During the deep learning modeling process, we performed feature pre-fusion using both ONS and MCASDI images. However, the pre-fused model did not outperform the ONS-based DLR model alone. We hypothesize two potential reasons for this outcome. First, ONS images were acquired using a high-resolution linear array probe, providing superior image quality compared to MCASDI images obtained with a lower-frequency convex array probe. The latter is affected by far-field attenuation and poor sound transmission through the temporal window. Additionally, studies have shown that the sensitivity of MCASDI in detecting IH is constrained by its SNR or CNR[21]. Second, the predictive value of certain indices, such as the PI for IH, may decrease in cases of mild IH[5]. Cerebral blood flow autoregulation—mediated by factors such as elevated PCO_2, decreased PO_2[22] and the accumulation of cellular metabolites[23]—helps maintain MCASDI within normal limits. Consequently, this results in an overlap between normal and mild IH in the DTL process.

In clinical practice, we collect patient data on ONSD and TCCD, with image segmentation performed by experienced physicians. Radiomic and deep learning features are then extracted using PyRadiomics and deep learning models, and these features are integrated into the predictive model. Although the model's efficiency is not yet sufficient for the direct diagnosis of early IH, it serves as a valuable tool for optimizing treatment strategies. On one hand, if the model predicts a high probability of early IH, it allows clinicians to promptly identify the underlying cause and implement appropriate measures to prevent brain herniation or irreversible damage. On the other hand, for patients initially predicted to have a high likelihood of IH, follow-up evaluations after treatment can help assess whether the risk has decreased, thereby aiding in the evaluation of treatment effectiveness. In summary, our model is expected to provide valuable guidance for personalized decision-making in the management of early IH.

This study has several limitations. First, its retrospective design may introduce potential selection bias; therefore, future research should validate the model's feasibility through prospective studies. Second, another important limitation of our study is the random allocation of patients between two medical centers without implementing center-based stratification. This approach may introduce potential data leakage and limit our ability to assess the true generalizability across different institutional settings. Future studies will employ leave-one-center cross-validation to better evaluate the model's generalizability. Third, discrepancies arose due to the subjective nature of boundary delineation during manual segmentation. Additionally, our DTL model did not show a significant advantage over traditional radiomics and clinical models, which may be attributed to the manual delineation of ROIs. Future research should explore the optimal size and range of ROIs to enhance the DTL model's predictive capability. Fourth, unlike typical TBI cases, post-DC TBI patients do not strictly adhere to the Monro-Kellie doctrine[24],, and their ICP thresholds remain undefined. Therefore, additional parameters, such as surgical incision size, operation duration, and blood loss, may be necessary for more precise classification and evaluation. Fifth, this study lacked completely external validation using datasets from other institutions due to the limited availability of post-DC patients with invasive ICP monitoring. We recognize the importance of external validation for evaluating model generalizability, and future work will aim to include multicenter data

for this purpose. Finally, this study focused exclusively on post-DC TBI patients and did not include other forms of IH unrelated to DC. Future studies should aim to extract features from different IH subtypes to develop tailored predictive models for each condition. Our findings underscore the potential of integrating DLR features into non-invasive ICP monitoring, particularly through high-quality ONS ultrasound images. Future research should focus on refining multimodal imaging approaches and expanding datasets to improve model robustness and clinical applicability.

Conclusion

Our study introduced and validated an integrated model that combines clinical-ultrasonic features, radiomics, and DTL features for the early detection of IH in post-DC TBI patients at different ICP thresholds using post-DC ultrasound images. This model presents a novel approach to precision medicine, with the potential to enhance clinical decision-making and improve patient outcomes during the critical period. Notably, concatenation-based feature pre-fusion of ONS and MCASDI images did not yield a substantial improvement in predictive performance, suggesting that ONS-derived features alone may be sufficient for early IH prediction.

Data availability

The datasets used and/or analysed during the current study are provided within the supplementary information files.

Received: 10 April 2025; Accepted: 25 June 2025
Published online: 02 July 2025

References

1. Raboel, P. H. et al. M,. Intracranial pressure monitoring: invasive versus non-invasive methods: a review. *Crit. Care Res. Pract.* **2012**, 950393. (2012).
2. Stevens, A. R. et al. Optical pupillometry in traumatic brain injury: neurological pupil index and its relationship with intracranial pressure through significant event analysis. *Brain Inj.* **33** (8), 1032–1038 (2019).
3. Faria, B. C. D. et al. The use of noninvasive measurements of intracranial pressure in patients with traumatic brain injury: a narrative review. *Arq. Neuropsiquiatr.* **81** (6), 551–563 (2023).
4. Harary, M., Dolmans, R. G. F. & Gormley, W. B. Intracranial pressure Monitoring-Review and avenues for development. *Sens. (Basel)*, **18**(2). (2018).
5. Rasulo, F. A. et al. Transcranial doppler as a screening test to exclude intracranial hypertension in brain-injured patients: the IMPRESSIT-2 prospective multicenter international study. *Crit. Care*. **26** (1), 110 (2022).
6. Robba, C. Measuring optic nerve sheath diameter using ultrasonography for the detection of Non invasive intracranial pressure: what it is and what it is not. *Arq. Neuropsiquiatr.* **80** (6), 547–549 (2022).
7. Robba, C. et al. Multimodal non-invasive assessment of intracranial hypertension: an observational study. *Crit. Care*. **24** (1), 379 (2020).
8. Brain Trauma, F. et al. Guidelines for the management of severe traumatic brain injury. V. Deep vein thrombosis prophylaxis. *J. Neurotrauma*. **24** (Suppl 1), S32–S36 (2007).
9. Demetriades, A. K. Intracranial pressure monitoring after primary decompressive craniectomy: is it useful? *Acta Neurochir. (Wien)*. **159** (4), 623–624 (2017).
10. Picetti, E. et al. Intracranial pressure monitoring after primary decompressive craniectomy in traumatic brain injury: a clinical study. *Acta Neurochir. (Wien)*. **159** (4), 615–622 (2017).
11. Chesnut, R. M. et al. A trial of intracranial-pressure monitoring in traumatic brain injury. *N Engl. J. Med.* **367** (26), 2471–2481 (2012).
12. Melhem, S., Shutter, L. & Kaynar, A. A trial of intracranial pressure monitoring in traumatic brain injury. *Crit. Care*. **18** (1), 302 (2014).
13. Fu, Z. et al. Post-craniotomy intracranial pressure monitoring: a novel approach combining optic nerve sheath diameter ultrasonography and cervical-cerebral arterial ultrasound. *Front. Neurol.* **15**, 1472494 (2024).
14. Lambin, P. et al. Radiomics: the Bridge between medical imaging and personalized medicine. *Nat. Rev. Clin. Oncol.* **14** (12), 749–762 (2017).
15. Song, J. et al. A new approach to predict Progression-free survival in stage IV EGFR-mutant NSCLC patients with EGFR-TKI therapy. *Clin. Cancer Res.* **24** (15), 3583–3592 (2018).
16. Dong, D. et al. Deep learning radiomic nomogram can predict the number of lymph node metastasis in locally advanced gastric cancer: an international multicenter study. *Ann. Oncol.* **31** (7), 912–920 (2020).
17. Jiang, Y. et al. Predicting peritoneal recurrence and disease-free survival from CT images in gastric cancer with multitask deep learning: a retrospective study. *Lancet Digit. Health*. **4** (5), e340–e50 (2022).
18. Fernando, S. M. et al. Diagnosis of elevated intracranial pressure in critically ill adults: systematic review and meta-analysis. *BMJ* **366**, l4225 (2019).
19. Wang, J. et al. Ultrasonographic optic nerve sheath diameter correlation with ICP and accuracy as a tool for noninvasive surrogate ICP measurement in patients with decompressive craniotomy. *J. Neurosurg.* **133** (2), 514–520 (2020).
20. Xu, X. et al. Diagnostic value of the combination of ultrasonographic optic nerve sheath diameter and width of crural cistern with respect to the intracranial pressure in patients treated with decompressive craniotomy. *Neurocrit Care*. **39** (2), 436–444 (2023).
21. Rondagh, M. et al. A comparison of ultrafast and conventional spectral doppler ultrasound to measure cerebral blood flow velocity during inguinal hernia repair in infants. *J. Clin. Anesth.* **92**, 111312 (2024).
22. Yoshihara, M., Bandoh, K. & Marmarou, A. Cerebrovascular carbon dioxide reactivity assessed by intracranial pressure dynamics in severely head injured patients. *J. Neurosurg.* **82** (3), 386–393 (1995).
23. Gordon, G. R. et al. Brain metabolism dictates the Polarity of astrocyte control over arterioles. *Nature* **456** (7223), 745–749 (2008).
24. Benson, J. C. et al. The Monro-Kellie doctrine: A review and call for revision. *AJNR Am. J. Neuroradiol.* **44** (1), 2–6 (2023).

Acknowledgements

We express our gratitude to all colleagues who provided assistance during the course of this study.

Author contributions

ZF.F: Conceptualization, Methodology, Writing – original draft, Writing – review & editing. J.W: Conceptualization, Methodology, Writing – original draft, Writing – review & editing. WY.S: Methodology, Writing – original draft. YQ.W: Formal Analysis, Software, Writing – original draft. JJ. Z: Formal Analysis, Software, Writing – original draft. Y.L: Software, Writing – original draft. CQ.W: Software, Writing – original draft. YL.S: Software, Writing – original draft. Y.Z: Software, Writing – original draft. WF.Z: Investigation, Supervision, Writing – original draft. CJ.L: Conceptualization, Funding acquisition, Project administration, Writing – original draft, Writing – review & editing. L.P: Conceptualization, Project administration, Writing – original draft, Writing – review & editing.

Declarations

Competing interests

The authors declare no competing interests.

Ethical approval and consent to participate

The study was conducted in accordance with the Declaration of Helsinki and approved by the Ethics Committee of the Second affiliated Hospital of Shandong First Medical University (2021-A-037).

Consent for publication

All authors agree to publish this paper.

Additional information

Supplementary Information The online version contains supplementary material available at https://doi.org/10.1038/s41598-025-09115-7.

Correspondence and requests for materials should be addressed to C.L. or L.P.

Reprints and permissions information is available at www.nature.com/reprints.

Publisher's note Springer Nature remains neutral with regard to jurisdictional claims in published maps and institutional affiliations.